Cortical Surface Shape Analysis Based on Alexandrov Polyhedra

Min Zhang[*1], Yang Guo[*2], Na Lei[†3], Zhou Zhao[2], Jianfeng Wu[4], Xiaoyin Xu[1], Yalin Wang[4], and Xianfeng Gu[2]

[1]Brigham and Women's Hospital, Harvard Medical School
[2]Stony Brook University
[3]Dalian University of Technology
[4]Arizona State University

Abstract

Shape analysis has been playing an important role in early diagnosis and prognosis of neurodegenerative diseases such as Alzheimer's diseases (AD). However, obtaining effective shape representations remains challenging. This paper proposes to use the Alexandrov polyhedra as surface-based shape signatures for cortical morphometry analysis. Given a closed genus-0 surface, its Alexandrov polyhedron is a convex representation that encodes its intrinsic geometry information. We propose to compute the polyhedra via a novel spherical optimal transport (OT) computation. In our experiments, we observe that the Alexandrov polyhedra of cortical surfaces between pathology-confirmed AD and cognitively unimpaired individuals are significantly different. Moreover, we propose a visualization method by comparing local geometry differences across cortical surfaces. We show that the proposed method is effective in pinpointing regional cortical structural changes impacted by AD.

1. Introduction

Alzheimer's disease (AD) is the most common type of dementia. It is commonly agreed that an effective presymptomatic diagnosis and treatment of AD could have enormous public health benefits [15]. Brain structural magnetic resonance imaging (sMRI) research has the potential to provide valid diagnostic biomarkers of AD risk factors. Although brain structural volumes are the most commonly used sMRI measures in AD research, surface-based brain structural measures offer more detailed and patient-specific shape information [21, 14, 2, 25]. Overall, a geometrically

---

[*]These two authors have equal contribution.
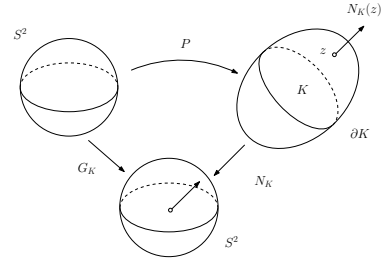
[†]Corresponding author

Figure 1: The Minkowski Problem

solid method, which is sensitive to intrinsic surface geometric features, is vital to identify reliable imaging biomarkers, reduce the sheer number of statistical tests, and thereby improve the statistical power of imaging analysis.

It is well known that a general surface in $\mathbb{R}^3$ is fully determined by its first fundamental form (Riemannian metric) and the second fundamental form, unique up to a rigid motion. Closed convex surfaces are solely determined by their Riemann metrics. According to Gauss's Theorema Egregium, the Gaussian curvature is intrinsically determined by the Riemannian metric. Therefore, given a surface, it is natural to ask whether its Gaussian curvature could be encoded into a convex shape, which enables us to visualize the Riemannian metric of the input surface, and helps us compare the Riemannian metric of the given surface to other surfaces.

The existence and computation of such a convex shape representation relates to the Minkowski problem and the Minkowski theorem. Mathematically, the *Minkowski problem (type II)* asks how to reconstruct a convex shape that fulfils a given Gaussian curvature measure. As shown in Fig. 1, the setup for the Minkowski problem is as follows: A domain $K \in \mathbb{R}^3$ is convex and contains the origin O. The boundary ∂K is a smooth convex surface, with polar coor-

dinate representation $\{\rho(x)x \mid x \in \mathbb{S}^2,\ \rho : \mathbb{S}^2 \to \mathbb{R}^+\}$ and the corresponding polar map $P : \mathbb{S}^2 \to \partial K$, $x \mapsto \rho(x)x$. The normal mapping $N_K := \partial K \to \mathbb{S}^2$ maps each point on ∂K to its normal vector. Now, the composition map $G_K := N_K \circ P$ is a mapping from $\mathbb{S}^2$ to $\mathbb{S}^2$. If we denote the Hausdorff measure (i.e., area element) on the image domain $\mathbb{S}^2$ as $\mathcal{H}^2$, then G_K pulls back $\mathcal{H}^2$ to the domain $\mathbb{S}^2$ and the pulled-back measure $(G_K)_\# \mathcal{H}^2$ is called the *Gaussian curvature measure*, denoted as ν. The Minkowski problem asks *how to find the shape of ∂K from the Gaussian curvature measure ν*. In fact, G_K is the unique optimal transportation (OT) map between $\mathcal{H}^2$ and ν, and therefore, the Minkowski problem is equivalent to solving a spherical OT problem, i.e., finding the most economical way on the sphere surface to transport the source measure $\mathcal{H}^2$ to the target measure ν under a prescribed cost function. For the Minkowski problem, the transportation cost is related to the spherical geodesic distance. According to Monge-Kantorovich theory, this is reduced to finding a pair of convex potential functions, which are Legendre dual to each other. Furthermore, the Kantorovic potential satisfies the spherical Monge-Ampère PDE. In discrete cases where the input surface is represented as a triangle mesh, the classical smooth solution can be approximated by weak solutions, i.e., the Alexandrov solutions, which are convex polyhedra and C^1 converges to the smooth solution.

In this work, we prove the existence of the solution to the Minkowski problem based on Monge-Kantorovich theory (see e.g., [23]). The proof leads to a rigorous and practical algorithm to compute the Alexandrov polyhedron using a variational approach in the discrete case. Furthermore, the obtained Alexandrov polyhedron can be applied as a shape signature of the original surface. Our experiments show that the Hausdorff distances between Alexandrov polyhedra of the brain cortical surfaces from AD patients and cognitively unimpaired (CU) individuals have significant group differences. Also, by comparing the shapes of Alexandrov polyhedra, we can pinpoint the AD-impacted brain regions that have significant geometric changes. These results show that the Alexandrov polyhedra are effective and accurate as shape signatures in capturing and visualizing geometric structural changes of brain cortical surfaces affected by early AD. Moreover, we base the computation of Alexandrov polyhedra on computing intrinsic spherical optimal transport maps, where novel mathematical formula and algorithms are used to improve efficiency.

Related Works Since the cortical surface is topologically equivalent to a sphere, shape analysis and classification methods based on spherical harmonic map and optimal transport map have been extensively studied [8, 18, 20, 16, 22]. In works [3, 4, 9] various rigid and non-rigid surface registration approaches have been studied. In [8], the authors proposed using spherical harmonic maps to regis-

ter brain cortical surfaces on the unit sphere. A spherical harmonic map provides a diffeomorphism for convex domains, has clear physical interpretation of minimizing elastic energy of the deformation, and can be computed by efficient algorithms [24, 26, 17]. However, conformal maps are prone to cause large area distortions if the geometry of the input surface is complicated. This decreases the robustness of registration and shape analysis in the parameterization domain. To mitigate this problem, area-preserving maps have been proposed for brain cortical analysis [18, 12]. In [20], Su et al. proposed a shape classification method on brain cortical surfaces of various intelligence quotients using Wasserstein distance. Similar to our proposed method, they also computed the spherical power diagram and optimal transport map to compare brain structural differences. But the computation of optimal transport map uses stereographic projection from the sphere to the 2D plane, where Euclidean metrics are used, making the result dependent on the choice of the north pole and not intrinsic to spherical Riemannian metric. Later in [12], a divide-and-conquer method was proposed. Specifically, the sphere is first sliced into two hemispheres, which are treated separately, and then wielded together using conformal wielding techniques. However, the result of this method depends on the choice of the cutting locus. In our method, we directly compute the optimal transport map on the sphere using intrinsic spherical Riemannian metric and is thus independent of initial conditions. Recently, in [6], the authors studied the spherical optimal transport using spherical Riemannian metric, and they proposed to use Monge-Kantorovich theory to compute the intrinsic spherical optimal transport map. In particular, the OT map is computed via optimizing a convex functional energy. Compared to this work, we use a novel formulation of the energy gradient and Hessian, which avoids the computation of the power radii. Furthermore, we propose a novel Lawson's edge flip to handle the mesh connectivity changes during the mesh updating step. This avoids reconstructing the entire mesh at each of the optimization steps, and thus improves the efficiency. In addition, besides a uni-variate biomarker that related works mainly focused on (e.g., the Wasserstein distance [20]), our method provides a shape signature for each cortical surface, which contains more information in capturing and pinpointing subregional shape structure differences.

Contributions In summary, the main contributions of this paper are as follows. 1) By adopting the Kantorovich dual framework, we propose a novel formulation that leads to a rigorous and practical computational method for spherical optimal transport problem, which is intrinsic to the spherical geometry. 2) We propose a novel generalized Lawson's edge flip method to improve computational efficiency. 3) We propose to use the Alexandrov polyhedra as a novel shape signature of the brain surface. Its effectiveness is

demonstrated in detecting brain structural changes affected by AD. Furthermore, our proposed method is general and applicable to any closed genus-0 surfaces.

2. Theory

2.1. Minkowski Problem for Curvature Measures

Let $K \subset \mathbb{R}^d$ be an open bounded convex domain containing the origin, and we parameterize ∂K in *polar coordinates* as follows: $\partial K = \{\rho(x)x \mid x \in \mathbb{S}^{d-1}, \rho : \mathbb{S}^{d-1} \to \mathbb{R}^+\}$. Then to any point $z \in \partial K$, we associate the *normal mapping* $N_K(z) := \{y \in \mathbb{S}^{d-1} | K \subset \{w \in \mathbb{R}^d \mid \langle y, w - z \rangle \leq 0\}\}$. Geometrically, the normal mapping finds the normals of all supporting hyperplanes at z (Fig. 2(a)).

Definition 1 (Gauss Map and Gaussian Measure). The (multivalued) *Gauss map* $G_K : \mathbb{S}^{d-1} \to \mathbb{S}^{d-1}$ is defined by $G_K(x) := N_K(\rho(x)x)$, and define the *Gaussian curvature measure* $\mu_K(E) := \mathcal{H}^{d-1}(G_K(E))$, for all measurable set $E \subset \mathbb{S}^{d-1}$, where $\mathcal{H}^{d-1}$ denotes the $(d-1)$-dimensional Hausdorff measure on $\mathbb{S}^{d-1}$.

Problem (Minkowski). Given a finite measure ν on $\mathbb{S}^{d-1}$, can one find an open bounded convex set K containing the origin such that $\nu = \mu_K$?

Definition 2 (Spherical convex set and polar set). Let $\omega \subset \mathbb{S}^{d-1}$, we say that ω is convex if the cone $\mathbb{R}^+\omega := \{tx : t > 0, x \in \omega\}$ is convex. We define the polar set to ω as $\omega^* := \{y \in \mathbb{S}^{d-1} \mid \langle x, y \rangle \leq 0 \quad \forall x \in \omega\}$.

Theorem 1 (Minkowski [5]). Let ν be a finite measure on $\mathbb{S}^{d-1}$. Then

$$\nu = \mu_K \text{ for some } K$$
$$\iff \begin{cases} (a) & \nu(\mathbb{S}^{d-1}) = \mathcal{H}^{d-1}(\mathbb{S}^{d-1}) \\ (b) & \nu(\mathbb{S}^{d-1} \setminus \omega) > \mathcal{H}^{d-1}(\omega^*) \\ & \forall \omega \subsetneq \mathbb{S}^{d-1} \quad \text{compact and convex} \end{cases}$$

Also, if K exists, then it is unique up to a dilation.

Up to a change of coordinates, we can write ∂K as the graph of a convex function $u : \Omega \subset \mathbb{R}^d \to \mathbb{R}$. Suppose u is C^2, then the Gaussian curvature of the graph of u is $\frac{det D^2 u}{(1+|\nabla u|^2)^{(d+2)/2}}$. This shows that solving the Minkowski problem is equivalent to a Monge-Ampère type PDE. Suppose $\mu_K = f d\mathcal{H}^2$, where the density function f is bounded. By the regularity theory, the boundary ∂K is C^1. Therefore, determining the boundary of K is equivalent to finding an optimal transport map $T : \mathbb{S}^{d-1} \to \mathbb{S}^{d-1}$ that transports $\mathcal{H}^{d-1}$ to ν.

Definition 3 (Generalized Legendre Dual). Given a convex hypersurface in $\mathbb{R}^d$ with polar representation $S_\rho := \{\rho(x)x \mid x \in \mathbb{S}^{d-1}, \rho : \mathbb{S}^{d-1} \to \mathbb{R}^+\}$, its generalized

Legendre dual (Fig. 2(b)) is $S_\rho^* := \{h(y)y \mid y \in \mathbb{S}^{d-1}, h : \mathbb{S}^{d-1} \to \mathbb{R}^+\}$, where

$$h(y) := \sup_{x \in S} \rho(x)\langle x, y \rangle. \tag{1}$$

Suppose $\varphi(x) := \log \rho(x)$, $\psi(y) := -\log h(y)$, the cost function $c(x, y) := -\log\langle x, y \rangle$, then the (spherical) *c-transform* is defined as $\varphi^c(y) := \inf_{x \in \mathbb{S}^{d-1}} c(x, y) - \varphi(x)$. A straightforward computation shows that performing c-transform on φ is equivalent to performing generalized Legendre dual on ρ.

In the following, we give a proof for the existence of K, which leads to a computational algorithm for the discrete case.

Proof. The Minkowski problem can be reformulated as an optimal transport problem: given a finite measure ν on $\mathbb{S}^{d-1}$, find an optimal transport map $T : \mathbb{S}^{d-1} \to \mathbb{S}^{d-1}$ that minimizes

$$\inf_{T_\# \mathcal{H}^{d-1} = \nu} \int_{\mathbb{S}^{d-1}} -\log\langle x, T(x) \rangle d\mathcal{H}^{d-1}.$$

One can verify that the optimized T is the desired G_K (see definition 1) such that $\mu_K = \nu$. Moreover, the minimization problem is equivalent to its Kantorovich dual problem: $\sup_{\varphi, \psi} \{I(\varphi, \psi), (\varphi, \psi) \in \mathcal{A}\}$, where the functional is defined as

$$I(\varphi, \psi) = \int_{\mathbb{S}^{d-1}} \varphi(x) d\nu(x) + \int_{\mathbb{S}^{d-1}} \psi(y) d\mathcal{H}^{d-1}(y) \tag{2}$$

and the admissible function space is

$$\mathcal{A} := \{(\varphi, \psi) \in (C(\mathbb{S}^{d-1}), C(\mathbb{S}^{d-1})) \\ \mid \varphi(x) + \psi(y) \leq c(x, y)\}. \tag{3}$$

One can construct a sequence of function pairs $\{(\varphi_k, \psi_k)\} \subset \mathcal{A}$, where $\psi_k = \varphi_k^c$ and $\varphi_k = \psi_{k-1}^c$. A straightforward computation shows that $I(\varphi_k, \psi_k)$ increases monotonically, and φ_k, ψ_k are Lipschitz continuous, with Lipschitz constant $\beta = \sup\{|Dc(x, y)|, x, y \in \mathbb{S}^{d-1}\}$. By Lipschitz continuity, we get $\{\psi_k\}$ are uniformly bounded, hence $\{\varphi_k\}$ are also uniformly bounded. By the Arzelà-Ascoli theorem, up to a subsequence, (φ_k, ψ_k) uniformly converge to (φ^*, ψ^*), which is Lipschitz continuous and maximizes the functional. This proves the existence. $\square$

2.2. Discrete Minkowski Problem

In practice, we focus on the two-dimensional unit sphere $\mathbb{S}^2$ situation. We derive the discrete Minkowski problem and generalize theorem 1 to the discrete case.

Suppose $K \subset \mathbb{R}^3$ is a compact convex set, its boundary ∂K is a convex triangular mesh. Assume the vertices of the
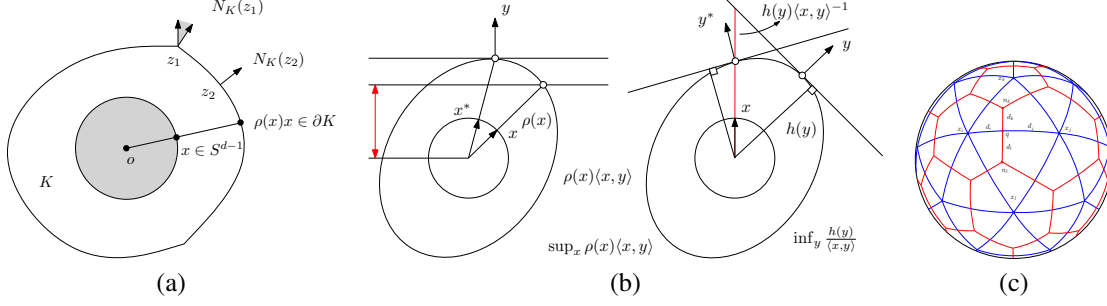
Figure 2: (a) Normal Mapping. (b) Generalized Legendre dual: given a surface $S_\rho = \rho(x)x$ and a unit vector y, $h(y)$ is the height of the unique plane with normal vector y and tangent to S_ρ (left), and such planes form an envelope of S_ρ (right). (c) Power diagram (red) and weighted Delaunay (blue).

polyhedron are $v_1, v_2, \cdots, v_n$, then ∂K is the convex hull of its vertices $\partial K = \mathrm{Conv}(\{v_i\}_{i=1}^n)$. The normal mapping maps each vertex v_i to a geodesic convex polygon $N_\rho(v_i)$ on the sphere, and the spherical area of $N_\rho(v_i)$ is the (discrete) *Gaussian curvature measure* of v_i.

Suppose the polar coordinate of each v_i is $v_i = \rho_i x_i$ where $\rho_i > 0$ is the radius of the polar coordinate of v_i and x_i is the unit vector in the direction of v_i. Then the generalized Legendre dual $\eta(y)$ of $\rho(x)$ can be computed as

$$\eta(y) := \min_{i=1}^{k} \left\{ \frac{1}{\rho_i} \frac{1}{\langle x_i, y \rangle} \right\}. \tag{4}$$

On the right hand side, each $1/(\rho_i \langle x_i, y \rangle)$ is a plane in $\mathbb{R}^3$, denoted as π_{x_i, ρ_i} with normal x_i and height $1/\rho_i$. The radial graph S_ρ^* is the inner envelope of these planes, $S_\rho^* = \mathrm{Env}(\{\pi_{x_i, \rho_i}\}_{i=1}^n)$. The center projection of S_ρ^* onto $\mathbb{S}^2$ induces a spherical power diagram (Fig. 2(c)), with each face of S_ρ^* projected to a spherical convex polygons $W_i(\rho)$,

$$\mathbb{S}^2 = \bigcup W_i(\rho), \quad W_i(\rho) := \{y \in \mathbb{S}^2 \mid \pi_{x_i, \rho_i}(y) \le \pi_{x_j, \rho_j}(y)\}. \tag{5}$$

Note that $y \in W_i(\rho)$ is equivalent to $\rho_i \langle x_i, y \rangle \ge \rho_j \langle x_j, y \rangle$, $\forall j$, namely $y \in N_\rho(v_i)$. Therefore the cell W_i equals to the normal mapping image of v_i, $W_i(\rho) = N_\rho(x_i)$, and the spherical area of $W_i(\rho)$ equals to the Gaussian curvature measure of v_i. Therefore, the discrete Minkowski problem can be formulated as follows:

Problem (Discrete Minkowski). Given distinct points $\{x_1, x_2, \cdots, x_n\}$ on $\mathbb{S}^2$ such that no hemisphere contains all the points, and positive discrete measures $\nu_1, \nu_2, \cdots, \nu_n > 0$ on each x_i with $\sum_{i=1}^n \nu_i = 4\pi$, find positive numbers $\rho = (\rho_1, \rho_2, \cdots, \rho_n)$ such that the each vertex $v_i := \rho_i x_i$ on the convex hull $S_\rho = \mathrm{Conv}(\{\rho_i x_i\}_{i=1}^n)$ has the Gaussian curvature measure equal to ν_i, $i = 1, 2, \cdots, n$.

The Minkowski theorem 1 can be generalized to the discrete situation directly, where the radius function ρ exists,

unique up to scaling, and S_ρ is called the *Alexandrov polyhedron*. In fact, the functional Eqn. (2) becomes to a simpler form in discrete case. In general, suppose μ is a finite measure with on the sphere with $\mu(\mathbb{S}^2) = 4\pi$ and has continuous density (the Hausdorff measure $\mathcal{H}^2$), $\varphi := \log \rho$, $\psi := \log \eta$, $\nu := \sum_{i=1}^n \nu_i \delta(y - x_i)$ and $w_i(\rho) := \mu(W_i(\rho))$, then

$$
\begin{aligned}
I(\varphi, \psi) &= \int_{\mathbb{S}^2} \varphi(x) d\nu(x) + \int_{\mathbb{S}^2} \psi(y) d\mu(y), \quad (\varphi, \psi) \in \mathcal{A} \\
&= \sum_{i=1}^n \int_{W_i(\varphi)} \varphi^c d\mu(x) + \sum_{i=1}^n \varphi_i \nu_i, \quad \varphi_i = \varphi(x_i), \\
&= \sum_{i=1}^n \int_{W_i(\varphi)} (c(x, x_i) - \varphi_i) d\mu(x) + \sum_{i=1}^n \varphi_i \nu_i \\
&= \sum_{i=1}^n \int_{W_i(\varphi)} c(x, x_i) d\mu(x) + \sum_{i=1}^n \varphi_i (\nu_i - w_i(\varphi)).
\end{aligned}
\tag{6}
$$

Since ν is a sum of Dirac measures, φ can be treated as a vector $(\varphi_1, \varphi_2, \ldots, \varphi_n)$. In the following lemma, we show the concavity of the energy (6), which can be optimized via Newton's method.

Lemma 2. Suppose $\varphi = (\varphi_1, \varphi_2, \ldots, \varphi_n)$. The gradient of the energy

$$I(\varphi_1, \cdots, \varphi_n) = \sum_{i=1}^n \int_{W_i(\varphi)} c(x, x_i) d\mu(x) + \sum_{i=1}^n \varphi_i (\nu_i - w_i(\varphi)) \tag{7}$$

is given by

$$\nabla I(\varphi) = (\nu_1 - w_1(\rho(\varphi)), \nu_2 - w_2(\rho(\varphi)), \cdots, \nu_n - w_n(\rho(\varphi))), \tag{8}$$

and off-diagonal and diagonal elements of its Hessian ma-

trix are

$$
\begin{cases}
\dfrac{\partial^2 I(\varphi)}{\partial \varphi_i \partial \varphi_j} &= -\dfrac{\partial w_i(\varphi)}{\partial \varphi_j} = -\dfrac{\partial w_j(\varphi)}{\partial \varphi_i} = \dfrac{\sin d_l + \sin d_k}{\tan d_i + \tan d_j} \\
\dfrac{\partial^2 I(\varphi)}{\partial \varphi_i^2} &= \sum_{j \neq i} \dfrac{\partial w_i(\varphi)}{\partial \varphi_j},
\end{cases}
\tag{9}
$$

where edge lengths of d_i's are depicted in Fig. 2(c). Furthermore, the null space of the Hessian is $\mathrm{Span}\{(1, 1, \cdots, 1)\}$, the energy is strictly concave on the complementary space of the null space.

Proof. Suppose two cells $W_i(\varphi)$ and $W_j(\varphi)$ intersect with each other. Let $\varphi' = \varphi + \delta e_i$, where e_i is the unit vector along the i-th coordinate axis. Then W_i enlarges, W_j shrinks. Suppose $x \in W_i(\varphi') \cap W_j(\varphi)$,

$$
x \in W_j(\varphi) \implies c(x, x_j) - \varphi_j \leq c(x, x_i) - \varphi_i
$$
$$
x \in W_i(\varphi') \implies c(x, x_j) - \varphi_j \geq c(x, x_i) - \varphi_i - \delta
$$

This shows $0 \leq (c(x, x_i) - \varphi_i) - (c(x, x_j) - \varphi_j) \leq \delta$. Then we compute

$$
I(\varphi') - I(\varphi) = -\delta w_i(\varphi) + \delta \nu_i +
$$
$$
\sum_{j \neq i} \int_{W_j(\varphi) \cap W_i(\varphi')} [(c(x, x_i) - \varphi_i - \delta) - (c(x, x_j) - \varphi_j))] d\mu(x)
$$
$$
= \delta(\nu_i - w_i(\varphi)) + \sum_{j \neq i} O(\delta) \mu(W_j(\varphi) \cap W_i(\varphi')). \tag{10}
$$

By direct deduction of lemma 4 in [6], we can obtain

$$
\frac{\partial w_j(\varphi)}{\partial \varphi_i} = \frac{\partial w_i(\varphi)}{\partial \varphi_j} = -\frac{\sin d_l + \sin d_k}{\tan d_i + \tan d_j}. \tag{11}
$$

Therefore we get $I(\varphi + \delta e_i) - I(\varphi) = \delta(\nu_i - w_i(\varphi)) + O(\delta^2)$, hence we obtain the gradient formula $\partial I(\varphi)/\partial \varphi_i = \nu_i - w_i(\varphi)$. Furthermore, $w_i(\varphi)$ is differentiable, and thus we obtain the formula for $\partial^2 I(\varphi)/\partial \varphi_i \partial \varphi_j$. Since

$$
0 = \frac{\partial 4\pi}{\partial \varphi_i} = \sum_{j=1}^n \frac{\partial w_j(\varphi)}{\partial \varphi_i} = \sum_{j=1}^n \frac{\partial w_i(\varphi)}{\partial \varphi_j},
$$

we obtain $\partial w_i(\varphi)/\partial \varphi_i = \sum_{j \neq i} \partial w_i(\varphi)/\partial \varphi_j$. By geometric meaning, $\partial w_j/\partial \varphi_i < 0$, hence the off diagonal elements of the Hessian matrix are non-negative. The Hessian matrix is diagonal dominant, hence its null space is one dimensional spanned by $(1, \ldots, 1)$. Otherwise, assume v is in the null space, the k-th element of v has the biggest absolute value, then the k-th element of $\mathrm{Hess} \cdot v$ is non-zero, contradiction. The Hessian matrix is negative definite on the complementary space of the null space, this implies the strict concavity of the energy. $\square$

Algorithm 1: Computing S_ρ

Input: Target measure $\nu = \sum_{i=1}^n \nu_i \delta(x - x_i)$, initial spherical triangulation $\mathcal{T}$
Output: The Alexandrov polyhedron S_ρ
Initialize φ_i's to be zeros, $\rho_i \leftarrow \exp(\varphi_i)$;
Initialize d to be zero, $\lambda \leftarrow 1$;
while *true* **do**
  repeat
    $\varphi \leftarrow \varphi + \lambda d$, $\rho \leftarrow \exp(\varphi)$;
    Use the generalized Lawson's edge flip [10] to update the convex hull S_ρ;
    $\lambda \leftarrow \frac{1}{2}\lambda$;
  until *no missing vertex on the convex hull*;
  Compute the Legendre dual S_ρ^*;
  Central project S_ρ and S_ρ^* to get $\mathcal{T}$ and $\mathcal{D}$;
  Compute the cell areas to get the gradient $\nabla I(\varphi)$ by Eqn. (8);
  if $\|\nabla I(\varphi)\| < \varepsilon$ **then**
    break;
  end
  Compute the edge lengths to get the Hessian matrix by Eqn. (9);
  Solve linear system $\mathrm{Hess}(\varphi)d = \nabla I(\varphi)$;
end
With the optimal φ, construct $S_\rho = \{\rho_i x_i\}$ with $\rho_i = \exp(\varphi_i)$;

---

3. Computational Algorithm

The pipeline of our proposed method consists of three major steps. First, given an input triangular mesh of a cortical surface $\mathcal{S}$ (Fig. 3 (a)), we conformally map $\mathcal{S}$ to $\mathbb{S}^2$ via a spherical harmonic map (Fig. 3 (d)). Second, on $\mathbb{S}^2$, we set the target measure ν_i at each vertex as the corresponding vertex area on $\mathcal{S}$ and compute the Alexandrov polyhedron S_ρ (Fig. 3 by solving the discrete Minkowski problem (Alg. 1). In particular, we optimize the energy Eqn. 7 with respect to ϕ, and at each step we measure the gradient by computing spherical cell areas of the power diagram $\mathcal{D}_\rho$ (Fig. 3 (f)). Finally, an area-preserving map from $\mathcal{S}$ to $\mathbb{S}^2$ is obtained by mapping each vertex in $\mathcal{S}$ to the center of cells in the power diagram. This map is intrinsic to the spherical Riemannian metric and thus provides an intrinsic registration among cortical surfaces [19] as well as corresponding Alexandrov polyhedra. The obtained area-preserving map and Alexandrov polyhedron provide novel and reliable biomarkers and visualization tools for brain cortical surface shape analysis purposes.

3.1. Spherical Harmonic Map

The spherical harmonic map $f_1 : \mathcal{S} \to \mathbb{S}^2$ is computed using the method in [8] (Fig. 3 (a) to Fig. 3 (d)). This map

(a) Input Surface $\mathcal{S}$ (b) Discrete Alex. Poly. S_ρ (c) Envelope S_ρ^*

(d) Harmonic Map   (e) Weighted Delaunay $\mathcal{T}_\rho$ (f) Power Diagram $\mathcal{D}_\rho$
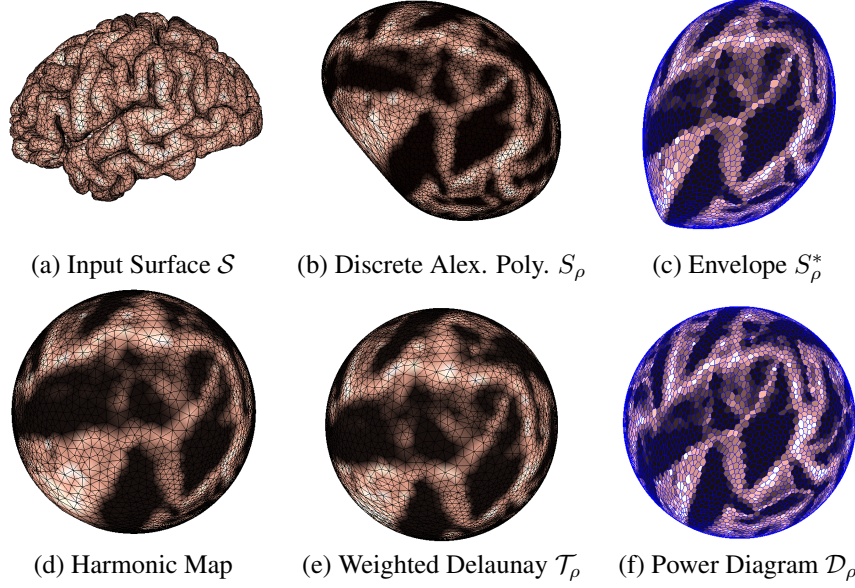
Figure 3: Cortical surface, harmonic map, Alexandrov polyhedron, the induced spherical weighted Delaunay triangulation, the generalized Legendre dual (i.e. the envelope), and the induced spherical power diagram.

is conformal, 1-to-1 continuous, and determined by the intrinsic geometry of the input surface, but the area at each vertex is potentially distorted.

3.2. Computing the Alexandrov Polyhedron S_ρ

Next, suppose each vertex $v_i \in \mathcal{S}$ is mapped to $x_i := f_1(v_i) \in \mathbb{S}^2$ under the spherical harmonic map, we set the target measure $\nu = \sum_{i=1}^n \nu_i \delta(x - x_i)$ with $\nu_i = \text{VertexArea}(v_i)$. Here $\text{VertexArea}(v_i)$ is the mean area of adjacent triangular faces of v_i in $\mathcal{S}$. Now we solve the discrete Minkowski problem via optimizing the discrete energy $I(\varphi)$ (Eqn. (7)) within the admissible solution space $\mathcal{A}$ (see Eqn. (3)). Since by lemma 2, the optimization is concave, it is optimized via Newton's method, using gradient Eqn. (8) and Hessian Eqn. (9). Specifically, to evaluate the gradient and Hessian, we need to compute the $w_i^{(k)}$ term from $\varphi_i^{(k)}$ at the k-th iteration. To do this, we first construct $S_{\rho^{(k)}}^* := \{\eta^{(k)}(y)y \mid y \in \mathbb{S}^2\}$ from $\varphi^{(k)}$ where $\rho^{(k)} = \exp \varphi^{(k)}$ and $\eta^{(k)}(y)$ is computed via the Legendre dual (Eqn. (4)). $S_{\rho^{(k)}}^*$ is then projected onto the unit sphere and forms a power diagram $\mathcal{D}_{\rho^{(k)}}$ (from Fig. 3 (e) to Fig. 3 (f)). Now $w_i(\rho^{(k)})$ is computed as $\text{Area}(W_i(\rho^{(k)}))$, where $W_i(\rho^{(k)})$ is the i-th cell of $\mathcal{D}_{\rho^{(k)}}$. With the gradient and Hessian, $\varphi_i^{(k)}$ is updated to $\varphi_i^{(k+1)}$ using the Newton's method. To deal with the mesh connectivity changes during this updating process, we propose for the first time to use Lawson's edge flip algorithm to maintain the convexity of S_ρ. This avoids reconstructing the whole mesh at each iter-

ations (see e.g., [6]). Details of the algorithm are in Alg. 1.

3.3. The Intrinsic Area-Preserving Map

In the previous step, the energy (Eqn. (6)) is optimized, which means the gradient of the energy (Eqn. (8)) equals to 0, i.e., for each cell W_i in $\mathcal{D}_\rho$, the area of W_i equals to $\nu_i = \text{VertexArea}(v_i)$. Therefore, the mapping between v_i to the geodesic center of the spherical polygon W_i forms an area-preserving map. We use thus obtained area-preserving maps to register all brain cortical surfaces, as well as their Alexandrov polyhedra. This registration is more robust than the one obtained using spherical harmonic maps [18].

3.4. Cortical Surface Shape Analysis

The obtained Alexandrov polyhedra and area-preserving map enable us to perform brain cortical surface shape analysis. In particular, given a dataset consisting of brain cortical surfaces, using the area-preserving map, we could perform an accurate registration among the brain surfaces. Then, using the corresponding Alexandrov polyhedra as shape representations of their Riemannian metric, we can measure the geometric differences and pinpoint regions that have significant changes.

The geometric intuition is that the Alexandrov polyhedron encodes the area density information of the input cortical surface. As shown in Fig. 4, the key observation is that if a vertex on the input surface has a higher vertex area, then the corresponding region of the Alexandrov polyhedron will has higher Gaussian curvature. Since the Alexan-
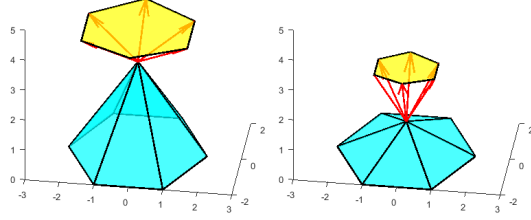
Figure 4: The blue polygon is a patch on the Alexandrov polyhedron. Red arrows are the adjacent face normals of the vertex. The yellow polygon is the image of the vertex under the normal mapping (see definition 1). The area of the yellow polygon equals to its vertex area on the input cortical surface. One observes that larger vertex area implies more "spikiness" on the Alexandrov polyhedron, and vice versa.

drov polyhedron is convex, this vertex will bump out. On the contrary, if a cortical surface region has a lower surface density relative to other parts (e.g., regional shrinkage caused by AD), then the corresponding region on its Alexandrov polyhedron tends to have lower Gaussian curvature. And because of the convexity, this region would be flatter than other parts. Furthermore, the difference of Alexandrov polyhedra from two surfaces can be measured using Hausdorff distance, since they are convex and registered. Here, the Hausdorff distance $d_h(X_1, X_2)$ of two sets $X_1, X_2 \subseteq \mathbb{R}^3$ is defined as $\max_{x \in X_1}(\min_{y \in X_2} d(x,y))$, where $d(\cdot, \cdot)$ is the Euclidean distance. Therefore, by computing the the Hausdorff distance of the Alexandrov polyhedra of two brain cortical surfaces, we can compare and visualize the difference between their Riemmanian metrics.

4. Experiments

In our experiments, we first compare our method with a previous spherical OT method in terms of accuracy and efficiency. We show that our method outperforms previous methods in terms of computation time and accuracy. Second, we demonstrate the capability of Alexandrov polyhedra as shape signatures in detecting AD-impacted brain morphometry changes.

4.1. Data Preparation

Brain sMRI data are obtained from the Alzheimer's Disease Neuroimaging Initiative (ADNI) database [11], from which we use 80 Aβ+ AD patients and 99 Aβ− CU subjects. Beta-amyloid (Aβ) positivity is determined by ADNI florbetapir positron emission tomography (PET) data. The PET images are processed using AVID pipeline [13] and later converted to centiloid scales. A centiloid cutoff of 37.1 is used to determine amyloid positivity [7]. The sMRIs are firstly preprocessed using FreeSurfer [1] to reconstruct the pial cortical surfaces, and we only use the left cerebral sur-
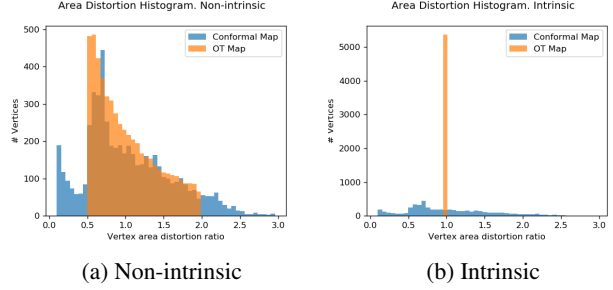

(a) Non-intrinsic   (b) Intrinsic

Figure 5: Spherical area distortion histograms computed via (a) non-intrinsic OT map [20] and (b) our method.

faces, which are topological spheres.

4.2. Computational Time

In this section, we compare the computational time between our method and the state-of-art intrinsic spherical OT algorithm [6]. Both of these methods compute spherical OT maps with spherical geodesic distances and spherical area forms (i.e. Hausdorff measure). The difference is that during the update process, we use the Lawson's edge flip algorithm that recover non-convex edges to convex ones locally, while the method in [6] reconstruct the whole mesh at each iteration. We implemented both of the algorithms in C++ and tested on our dataset (i.e., 179 cortical surfaces mapped to the unit sphere by conformal maps.). On a Intel core i5-4690 desktop with 16 GB RAM, the running time (mean and standard deviation) of our method is 16.11 ± 2.98 seconds, while the running time of the other method is 22.10 ± 0.65 seconds. This shows our proposed method is more efficient.

4.3. Intrinsic vs. Non-intrinsic Mapping

To check the accuracy difference between intrinsic and non-intrinsic spherical area-preserving maps, we compare the area distortion ratio of our method with the non-intrinsic one proposed in [20]. In particular, both methods compute the spherical optimal transport map. Composed with spherical conformal maps the goal of both methods is to form area-preserving maps from the input surface $\mathcal{S}$ to the unit sphere $\mathbb{S}^2$. The difference is that the method in [20] first maps the sphere onto the plane using stereographic projection, then computes area-preserving maps on the plane, and finally maps the result back using the inverse stereographic map. This steographic projection process potentially brings area distortion which makes the result less accurate. In our method, we directly compute the power diagrams on the sphere using spherical polygons and spherical area element (i.e., Hausdorff measure), thus avoids artificial area distortions. We compare the results from both methods in terms of area distortion ratios measured with the spherical Riemannian metric. Ideally, the ratios should concentrate near 1. In Fig. 5, the histograms of area distortion ratios show
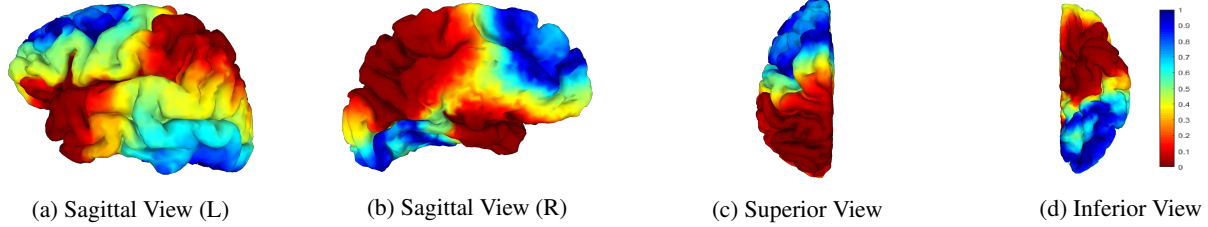
| (a) Sagittal View (L) | (b) Sagittal View (R) | (c) Superior View | (d) Inferior View |

Figure 6: Permutation test p-value heat map on the left cerebral cortical surface (deep red means significant shape difference).

Table 1: p-value comparison between different methods.

	Volume	Area	WD	APHD
p-value	0.703	0.486	0.580	**0.034**

that our method preserves spherical Riemannian metric and does not suffer from artificial area distortions.

4.4. Alexandrov Polyhedra in AD Detection

Group Difference Test In this experiment, to validate how well Alexandrov polyhedra is capable of differentiating geometries of different surfaces, we perform a non-parametric permutation test [21] on the Hausdorff distance of Alexandrov polyhedra between AD and CU groups. First, for each of the cortical surfaces from AD and CU groups, we compute the Hausdorff distance between their Alexandrov polyhedra and a fixed template Alexandrov polyhedron, which is computed from a randomly chosen cognitively unimpaired individual's cortical surface. We associate each cortical surface a response value, which equals to the Hausdorff distance between the sample and the template signature surfaces. We then perform a permutation test [25] on the group difference of the Hausdorff distance. In detail, we ran a permutation test with 5000 random assignments of subjects to groups to estimate the statistical significance of group mean differences. The randomization process here is important to remove biases from the results and the null hypothesis is that the two groups have the same mean. So the test statistic here is $|\mu_{\text{AD}} - \mu_{\text{CU}}|$. The output of the permutation test is the p-value, which measures the probability of obtaining the observed values assuming the null hypothesis is true. We then compare the p-value to a prior significance threshold, which is set as $p = 0.05$ in our experiment. We report that the p-value of the proposed method is 0.034, which is smaller than the threshold. So we reject the null hypothesis and accept the alternative, i.e., there is a significant group difference between the AD and CU groups. We compare different uni-variate biomarkers including shape volume, surface area, Wasserstein distance (WD) and the proposed Alexandrov polyhedron Hausdorff distance (APHD) with p-values under the same experiment settings (see Tab. 1). The result shows that while traditional biomarkers fail to detect the group difference, our proposed Alexandrov polyhedra based method is accurate in capturing the difference.

AD Impact Region Detection In this experiment we show the capability of using Alexandrov polyhedra to pinpoint and visualize subregional cortical surface changes impacted by AD. Specifically, given n cortical surfaces from both AD and CU groups, we compute their Alexandrov polyhedra and register the Alexandrov polyhedra $S_{\rho_i}^i$, $i = 1 \ldots n$ by their induced area-preserving maps (as discussed in section 3). From the registration, at each point $x_k \in \mathbb{S}^2$ on the unit sphere, we have a point set $\{v_k^1, v_k^2, \ldots, v_k^n\}$ for each of the n Alexandrov polyhedra, where $v_k^i = \rho_i(x_k)x_k$. On each v_k^i, we assign its radius $\rho_i(x_k)$ as the response value and perform permutation tests at each x_k. The output of the tests are p-values at each x_k. Thus the p-values form a function on $\mathbb{S}^2$. Since all brain cortical surfaces are registered are 1-to-1 mapped onto the unit sphere by the area-preserving maps, for visualization purpose, we plot the heat map of this p-value function on a randomly chosen template cortical surface $\mathcal{S}^0$ from the CU group in Fig. 6. The deep red regions correspond to significant group differences. As shown in Fig. 6, our method reveals significant differences in both temporal lobe and posterior cingulate, structures that are affected early by AD. The results demonstrate the capability of the proposed Alexandrov polyhedra in pinpointing geometric changes on the brain cortical surfaces impacted by AD.

5. Conclusion and Future Work

In this paper, we prove the existence of the solution to the discrete Minkowski problem based on Monge-Kantorovich theory. A novel algorithm is proposed to solve the discrete Minkowski problem with a novel explicit Hessian formula. Based on the solution to the discrete Minkowski problem, the Alexandrov polyhedron, we propose to use it as the shape signature of brain cortical surfaces and prove its accuracy in detecting structural changes of brain cortical surfaces impacted by AD. In the future, we plan to further study the effectiveness of the proposed shape signature method on other brain geometry impacting diseases.

References

[1] Freesurfer. https://surfer.nmr.mgh.harvard.edu/. 7

[2] L. G. Apostolova, P. M. Thompson, A. E. Green, K. S. Hwang, C. Zoumalan, C. R. Jack, D. J. Harvey, R. C. Petersen, L. J. Thal, P. S. Aisen, A. W. Toga, J. L. Cummings, and C. S. Decarli. 3D comparison of low, intermediate, and advanced hippocampal atrophy in MCI. *Hum Brain Mapp*, 31(5):786–797, May 2010. 1

[3] P. J. Besl and N. D. McKay. Method for registration of 3-d shapes. In *Sensor fusion IV: control paradigms and data structures*, volume 1611, pages 586–606. International Society for Optics and Photonics, 1992. 2

[4] A. M. Bronstein, M. M. Bronstein, and R. Kimmel. Generalized multidimensional scaling: a framework for isometry-invariant partial surface matching. *Proceedings of the National Academy of Sciences*, 103(5):1168–1172, 2006. 2

[5] S.-Y. Cheng and S.-T. Yau. On the regularity of the solution of the n-dimensional minkowski problem. *Communications on pure and applied mathematics*, 29(5):495–516, 1976. 3

[6] L. Cui, X. Qi, C. Wen, N. Lei, X. Li, M. Zhang, and X. Gu. Spherical optimal transportation. *Computer-Aided Design*, 115:181–193, 2019. 2, 5, 6, 7

[7] A. S. Fleisher, K. Chen, X. Liu, A. Roontiva, P. Thiyyagura, N. Ayutyanont, A. D. Joshi, C. M. Clark, M. A. Mintun, M. J. Pontecorvo, P. M. Doraiswamy, K. A. Johnson, D. M. Skovronsky, and E. M. Reiman. Using positron emission tomography and florbetapir F18 to image cortical amyloid in patients with mild cognitive impairment or dementia due to Alzheimer disease. *Arch Neurol*, 68(11):1404–1411, Nov 2011. 7

[8] X. Gu, Y. Wang, T. F. Chan, P. M Thompson, and S.-T. Yau. Genus zero surface conformal mapping and its application to brain surface mapping. *IEEE transactions on medical imaging*, 23(8):949–958, 2004. 2, 5

[9] S. Kurtek, E. Klassen, J. C. Gore, Z. Ding, and A. Srivastava. Elastic geodesic paths in shape space of parameterized surfaces. *IEEE transactions on pattern analysis and machine intelligence*, 34(9):1717–1730, 2011. 2

[10] C. L. Lawson. Transforming triangulations. *Discrete mathematics*, 3(4):365–372, 1972. 5

[11] S. G. Mueller, M. W. Weiner, L. J. Thal, R. C. Petersen, C. Jack, W. Jagust, J. Q. Trojanowski, A. W. Toga, and L. Beckett. The alzheimer's disease neuroimaging initiative. *Neuroimaging Clinics*, 15(4):869–877, 2005. 7

[12] S. Nadeem, Z. Su, W. Zeng, A. Kaufman, and X. Gu. Spherical parameterization balancing angle and area distortions. *IEEE transactions on visualization and computer graphics*, 23(6):1663–1676, 2016. 2

[13] M. Navitsky, A. D. Joshi, I. Kennedy, W. E. Klunk, C. C. Rowe, D. F. Wong, M. J. Pontecorvo, M. A. Mintun, and M. D. Devous. Standardization of amyloid quantitation with florbetapir standardized uptake value ratios to the Centiloid scale. *Alzheimers Dement*, 14(12):1565–1571, 12 2018. 7

[14] A. Qiu, C. Fennema-Notestine, A. M. Dale, and M. I. Miller. Regional shape abnormalities in mild cognitive impairment and Alzheimer's disease. *Neuroimage*, 45(3):656–661, Apr 2009. 1

[15] E. M. Reiman, J. Langbaum, A. S. Fleisher, R. J. Caselli, K. Chen, N. Ayutyanont, Y. T. Quiroz, K. S. Kosik, F. Lopera, and P. N. Tariot. Alzheimer's prevention initiative: a plan to accelerate the evaluation of presymptomatic treatments. *Journal of Alzheimer's Disease*, 26(s3):321–329, 2011. 1

[16] J. Shi and Y. Wang. Hyperbolic Wasserstein Distance for Shape Indexing. *IEEE Trans Pattern Anal Mach Intell*, 42(6):1362–1376, 06 2020. 2

[17] R. Shi, W. Zeng, Z. Su, H. Damasio, Z. Lu, Y. Wang, S.-T. Yau, and X. Gu. Hyperbolic harmonic mapping for constrained brain surface registration. In *Proceedings of the IEEE Conference on computer vision and pattern recognition*, pages 2531–2538, 2013. 2

[18] Z. Su, Y. Wang, R. Shi, W. Zeng, J. Sun, F. Luo, and X. Gu. Optimal mass transport for shape matching and comparison. *IEEE transactions on pattern analysis and machine intelligence*, 37(11):2246–2259, 2015. 2, 6

[19] Z. Su, W. Zeng, R. Shi, Y. Wang, J. Sun, and X. Gu. Area preserving brain mapping. In *Proceedings of the IEEE Conference on Computer Vision and Pattern Recognition*, pages 2235–2242, 2013. 5

[20] Z. Su, W. Zeng, Y. Wang, Z.-L. Lu, and X. Gu. Shape classification using wasserstein distance for brain morphometry analysis. In *International Conference on Information Processing in Medical Imaging*, pages 411–423. Springer, 2015. 2, 7

[21] P. M. Thompson, K. M. Hayashi, G. I. De Zubicaray, A. L. Janke, S. E. Rose, J. Semple, M. S¿ Hong, D. H. Herman, D. Gravano, D. M. Doddrell, et al. Mapping hippocampal and ventricular change in alzheimer disease. *Neuroimage*, 22(4):1754–1766, 2004. 1, 8

[22] Y. Tu, L. Mi, W. Zhang, H. Zhang, J. Zhang, Y. Fan, D. Goradia, K. Chen, R. J. Caselli, E. M. Reiman, X. Gu, and Y. Wang. Computing Univariate Neurodegenerative Biomarkers with Volumetric Optimal Transportation: A Pilot Study. *Neuroinformatics*, 18(4):531–548, 10 2020. 2

[23] C. Villani. *Optimal transport: old and new*, volume 338. Springer Science & Business Media, 2008. 2

[24] Y. Wang, M. Gupta, S. Zhang, S. Wang, X. Gu, D. Samaras, and P. Huang. High resolution tracking of non-rigid motion of densely sampled 3d data using harmonic maps. *International Journal of Computer Vision*, 76(3):283–300, 2008. 2

[25] Y. Wang, J. Zhang, B. Gutman, T. F. Chan, J. T. Becker, H. J. Aizenstein, O. L. Lopez, R. J. Tamburo, A. W. Toga, and P. M. Thompson. Multivariate tensor-based morphometry on surfaces: application to mapping ventricular abnormalities in hiv/aids. *NeuroImage*, 49(3):2141–2157, 2010. 1, 8

[26] D. Zhang and M. Hebert. Harmonic maps and their applications in surface matching. In *Proceedings. 1999 IEEE Computer Society Conference on Computer Vision and Pattern Recognition (Cat. No PR00149)*, volume 2, pages 524–530. IEEE, 1999. 2